Science Advances
AAAS

advances.sciencemag.org/cgi/content/full/6/22/eaay4945/DC1

Supplementary Materials for

Size-dependent influence of NO_x on the growth rates of organic aerosol particles

C. Yan*, W. Nie, A. L. Vogel, L. Dada, K. Lehtipalo*, D. Stolzenburg, R. Wagner, M. P. Rissanen, M. Xiao, L. Ahonen, L. Fischer, C. Rose, F. Bianchi, H. Gordon, M. Simon, M. Heinritzi, O. Garmash, P. Roldin, A. Dias, P. Ye, V. Hofbauer, A. Amorim, P. S. Bauer, A. Bergen, A.-K. Bernhammer, M. Breitenlechner, S. Brilke, A. Buchholz, S. Buenrostro Mazon, M. R. Canagaratna, X. Chen, A. Ding, J. Dommen, D. C. Draper, J. Duplissy, C. Frege, C. Heyn, R. Guida, J. Hakala, L. Heikkinen, C. R. Hoyle, T. Jokinen, J. Kangasluoma, J. Kirkby, J. Kontkanen, A. Kürten, M. J. Lawler, H. Mai, S. Mathot, R. L. Mauldin III, U. Molteni, L. Nichman, T. Nieminen, J. Nowak, A. Ojdanic, A. Onnela, A. Pajunoja, T. Petäjä, F. Piel, L. L. J. Quéléver, N. Sarnela, S. Schallhart, K. Sengupta, M. Sipilä, A. Tomé, J. Tröstl, O. Väisänen, A. C. Wagner, A. Ylisirniö, Q. Zha, U. Baltensperger, K. S. Carslaw, J. Curtius, R. C. Flagan, A. Hansel, I. Riipinen, J. N. Smith, A. Virtanen, P. M. Winkler, N. M. Donahue, V.-M. Kerminen, M. Kulmala, M. Ehn, D. R. Worsnop

*Corresponding author. Email: chao.yan@helsinki.fi (C.Y.); katrianne.lehtipalo@helsinki.fi (K.L.)

Published 27 May 2020, *Sci. Adv.* **6**, eaay4945 (2020)
DOI: 10.1126/sciadv.aay4945

This PDF file includes:

Supplementary Materials and Methods

1. Measurements

Measurement of sulfuric acid and gas-phase HOMs

Concentrations of sulfuric acid and highly oxygenated molecules (HOMs) are measured with a nitrate-ion based chemical ionization atmospheric pressure interface time-of-flight mass spectrometer (CI-APi-TOF) (*17, 34, 35*), which has been deployed in the previous CLOUD experiments and described in details in previous publications (*12, 14*). The nitrate ions are produced by exposing nitric acid (HNO_3)-containing sheath flow to soft x-ray radiation. These nitrate ions charge the analyte (e.g., H_2SO_4 or HOMs) in the drift tube, with a reaction time of 200 ms. After that, the sample flow enters the mass spectrometer, where it is focused in the APi module and analyzed in the TOF chamber based on the ion mass-to-charge ratio.

The raw data were processed with the MATLAB tofTools package (version 603)(*36*). The data were analyzed in high resolution mode that allowed peaks with different elemental formulae but under the same unit mass to be evaluated separately. Identified peaks were further grouped by their carbon number or nitrogen number (See Fig. 2).

To quantify sulfuric acid and HOMs, we calibrate the system with H_2SO_4 and correct the mass-dependent transmission. First, a general calibration coefficient is obtained for sulfuric acid. The OH concentration in the chamber is determined from an independent run using 1,3,5-trimethylbenzene. The production rate of sulfuric acid can be then calculated based on the OH and SO_2 concentrations in the chamber. Together with the well-characterized total sulfuric acid loss rate, the concentration is derived and the calibration coefficient can be obtained. We use this calibration coefficient for quantifying HOMs as well. In addition, corrections for the size-dependent ion transmission (*37*) and inlet sampling loss are applied. The overall uncertainty in the sulfuric acid and HOMs concentrations is estimated to be ca. 40 %, assuming a unit charging probability. However, recently studies have shown that the charging of HOMs by nitrate may vary considerably, depending on the functionality of HOMs (*38, 39*). Therefore, this method gives the lower bound of the HOM concentration. The uncertainty for relatively less oxidized HOMs needs further investigation.

Measurement of particle-phase products and their thermal desorption

Chemical analysis of the bulk particle-phase composition is performed using the Filter Inlet for Gases and Aerosols (FIGAERO)(*40*) coupled to an iodide-based chemical ionization time-of-flight mass spectrometer (CI-ToF-MS) (Tofwerk, HTOF). The measurement cycle involves particle sampling for 50 minutes at 8 SLPM (standard liters per min) sample flow, followed by a thermal desorption ramp (at the maximum heating rate) that reaches 100 °C

after three minutes, 130 °C after five minutes and 140 °C after ten minutes. This heating profile is sufficient for quantitative evaporation, as the ion-traces for low-volatility dimers are close to background levels after the ten-minute heating program. The filter is replaced between experiments, approximately every 48 hours, (Zefluor membrane, 2.0 µm pore size, 25 mm diameter, PALL, USA). The thermal desorption gas flow is 2 SLPM of ultrapure dry nitrogen. The iodide ions are produced by first passing dry nitrogen over a methyliodide permeation source (VICI International, USA) kept at 30 °C. The flow of 2.2 SLPM of the methyliodide/nitrogen reagent gas mixture then passes through a radioactive charge conditioner (210Po, 370 MBq, Model P-2021, NRD Inc., USA). The reagent gas is kept dry in order to maximize sensitivity toward organic acids (17). The IMR body is heated to approximately 50 °C to avoid condensation of low-volatility compounds; an active pressure control device (Aerodyne Inc., USA) maintained the pressure at 800 mbar. The instrument is calibrated with a mixture of organic acid standards, but the data shown here are only qualitative. Data analysis is performed with Tofware version 2.5.10_FIGAERO on 10 seconds average spectra. A post-acquisition mass calibration is conducted based on the ions I^-, $I(H_2O)^-$, $I(HNO_3)^-$ and I_3^-. Peak identification of the particle phase products is conducted by manual peak identification that allowed nC: 1-20, nH: 2-50, nO: 0-20. Based on different experimental conditions (both presence of NO_x and SO_2), the allowed number of nitrogen and sulfur is 0-2 and 0-1, respectively. Only elemental combinations of the neutral molecules having an integer double bond equivalent are considered. Overfitting of the peaks is avoided by allowing $\leq$ 4 molecular compositions per nominal mass. The appearance of organic nitrates and organic di-nitrates is closely observed with the increase of the NO_x levels during the experiment. The gas-phase adsorption on the filter is corrected by subtracting the adsorbed fraction from the measured intensity during the early stages of the experiment, when the gas-phase is in steady-state while particle mass was still building up. Gas-phase concentrations of the most of the oxidation products are too low throughout all experiments to be monitored in real-time by the gas-phase sampling position of the FIGAERO inlet.

In the thermos-desorption measurement for the T_{max} of HOM monomer, we noticed strong influence from the thermal decomposition of dimeric compounds, which also has been shown by Stolzenburg and co-workers (*41*). We commonly observed a bimodal character of the thermograms of several monomeric compounds (e.g. $C_{10}H_{16}O_4$, see Fig. S4). In this study (monoterpenes, NO_x, SO_2), it turns out that the complexity is increased, and we cannot rule out that thermal decomposition of organic sulfates and/or organic nitrates during the evaporation adds another dimension of complexity to the interpretation of thermograms. Therefore, we focused on the region of dimeric mass regions, in which we can exclude to introduce a bias that is caused by thermal decomposition.

Measurement of monoterpenes

The concentrations of monoterpenes and other volatile organic compounds (e.g. 1,3,5-trimethylbenzene) are measured with a newly-developed prototype of the proton transfer reaction time-of-flight mass spectrometer (PTR-TOF-MS; model: PTR3). Compared with the previous model, the PTR3 significantly improves the detection of low volatility compounds by reducing the sampling loss and increasing the sensitivity. More details about the instrument can be found elsewhere (*42*).

Measurement of Particle/ion number concentration and size distribution

The particle/ion concentration and number size distribution in the chamber are measured with several independent instruments. The particle size magnifier (PSM, Airmodus Ltd.) (*43*), coupled with a condensation particle counter (CPC) is used to determine the number concentration of the smallest particles. The PSM uses diethylene glycol (DEG) as working fluid at constant or varied supersaturation conditions achieved by tuning the mixing ratios between heated DEG-saturated air and the sample flow, which determines the instruments lower cut-off size. The external CPC is used to grow particles further with butanol and to determine their number concentration. In this study we use the scanning PSM to determine the particle concentration at several different cut-off sizes (1.7 nm used for nucleation rates), and the number size distributions between about 1.3 and 3 nm (*44*). In addition, several PSMs at fixed cut-off sizes and a conventional butanol ultra-fine CPC (TSI 3776) with a cut-off size of ca. 2.5 nm is used for comparison.

The size distribution of particles in the 1.9-7 nm size range was measured with the DMA-train (*45*). This is a recently developed instrument, consisting of six pairs of differential mobility analyzers (DMAs) and CPCs operated in parallel at fixed sizes. This method achieves a 100 % measurement duty cycle that allows exploitation of the full counting statistics at all six sizes, enabling high time-resolution and high sensitivity to low particle concentrations. Measurement of larger particles were conducted with a commercial nano-SMPS (TSI 3938) coupled with a water-CPC (TSI 3788), and a custom-built SMPS, consisting of a TSI X-ray source, a long DMA and a CPC (TSI 3010). Overall, the measured size distribution spans the range from about 1 to 500 nm.

A neutral cluster and air ion spectrometer (NAIS, Airel Ltd.) (*46*) was deployed to measure the ion concentrations and size distributions. It simultaneously determines the number size distribution of positive and negative ions in the range of 0.75 – 45 nm (ion mobility diameter) with two cylindrical mobility spectrometers in parallel, one for each polarity. Additionally, a corona unipolar charger is periodically switched on to charge the particles to enable measurement of the total particle size distribution over the 2–45 nm size range.

Measurement of other trace gases

Gas monitors are used to measure the concentration of sulfur dioxide (SO_2, ThermoFisher Scientific, Inc., model: 42i-TLE) and ozone (O_3, ThermoFisher Scientific, Inc., model: 49C). In addition, an accurate measurement of low-level nitrogen oxide (NO) concentrations is achieved with an advanced NO monitor (ECO PHYSICS, model: CLD 780 TR), which has a detection limit of ca. 3 pptv for a 1 min integration time. In all experiments reported here, NO is sampled from the middle of the chamber in the same way as the other gases. The NO mixing ratio close to its injection port is measured as about a factor of 5 higher. However, the space with highly concentrated NO should be very limited compared to the overall chamber volume; thus, the effect of this NO hotspot is neglected in this study. The concentration of nitrogen dioxide (NO_2) is measured with a cavity-attenuated phase-shift nitrogen dioxide monitor (CAPS NO_2, Aerodyne Research Inc.). The baseline signal is monitored periodically by flushing the inlet line with synthetic air. The NO_2 concentration is found to be similar when sampling from different ports, suggesting that the NO_2 concentration is homogeneous in the chamber.

2. Determination of particle nucleation rate and growth rate

The nucleation rates (J) are calculated from the time derivative of the total particle concentration and corrected for the particle losses in the chamber using the full size distribution.

$$J = \frac{dN}{dt} + S_{dil} + S_{wall} + S_{coag} \ (\mathrm{cm^{-3}\,s^{-1}}) \quad (1)$$

where N is the particle concentration above a certain cut-off size (d_p) to which the nucleation rate is calculated. The dilution correction S_{dil} arises from the fact that the chamber is constantly flushed with synthetic air to account for the instruments' sample flows.

$$S_{dil} = N \cdot k_{dil} \ (\mathrm{cm^{-3}\,s^{-1}}) \quad (2)$$

where $k_{dil} = 1.437 \times 10^{-4}\ \mathrm{s^{-1}}$ for CLOUD 10.

Diffusional losses to the chamber walls (S_{wall}) are determined empirically by observing the decay of the sulfuric acid monomer concentration in the chamber. The wall loss rate is inversely proportional to the particle size:

$$k_{wall}(d_p', T) = 2.116 \cdot 10^{-3} \cdot \left(\frac{T}{T_{ref}}\right)^{0.875} \cdot \left(\frac{d_{p,ref}}{d_p'}\right) (\mathrm{s^{-1}}) \quad (3)$$

where d_p' is the mobility diameter of the particle, $d_{p,ref}$ is the mobility diameter of the sulfuric acid monomer (= 0.82 nm), T_{ref} = 278 K, and T is the actual chamber temperature. Thus the total wall loss for particles larger than d_p is:

$$S_{wall}(d_p, T) = \sum_{d_p'=d_p}^{d_{p,max}'} N(d_p') \cdot k_{wall}(d_p', T) \ (\mathrm{cm^{-3}\,s^{-1}}) \quad (4)$$

Coagulation losses to the surface of larger aerosol particles (S_{coag}) are calculated from the measured number size distribution of particles present in the chamber

$$S_{coag}(d_{p,k}) = \sum_{d_{p,i}=d_{p,k}}^{d_{p,max}} \sum_{d_{p,j}=d_{p,i}}^{d_{p,max}} \delta_{i,j} \cdot K(d_{p,i}, d_{p,j}) \cdot N_i \cdot N_j \ (\mathrm{cm^{-3}\,s^{-1}}) \qquad (5)$$

where $K(d_{p,i},d_{p,j})$ is the coagulation coefficient for particles of size $d_{p,i}$ and $d_{p,j}$, N_i and N_j are the number densities of particles in a size bins i and j, and $\delta_{i,j} = 0.5$, if i = j and $\delta_{i,j} = 1$, if $i \neq j$.

The nucleation rates at 1.7 nm ($J_{1.7}$) are calculated from the scanning PSM and verified against the values calculated from the two other PSMs and the butanol CPC at fixed cut-off sizes. It should be noted that there is an uncertainty of about 0.5 nm in the cut-off size of the particle counters due to the effect of composition and charge on the detection efficiency (*47*). To account for this, we verify the cut-off size of the PSM for each chemical system in the chamber by comparing the concentration and rising time of the PSM at different saturator flow rates against the different size bins of the NAIS, which has been shown to be very accurate in determining the ion mobility. The *J* value given for each experiment is the median value after reaching stable conditions

The growth rates are calculated using the appearance time (*48*), as shown in Fig. 1b (the white dots). The appearance time at each particle size is defined as the time when particle concentration at a certain size reaches half of its maximum concentration. To exclude the systematic difference between these instruments, the appearance time from different instruments are checked for consistency in overlapping size regions, including the scanning PSM (1.3 – 2.3 nm), the DMA-train (1.9 – 3.5 nm and 3.5 – 7 nm), NAIS (2 – 40 nm), the nano-SMPS (4 – 30 nm), and the SMPS (>30 nm). In principle, the growth rate can be determined at any size, but, in practice, we fit the growth rate using the data from individual instruments at six fixed size ranges; these are 1.3 – 2.3 nm, 1.9 – 3.5 nm, 3.5 – 7 nm, 7 – 20 nm, 20 – 30 nm and >30 nm. It should be noted that the growth rates in the smallest size ranges are difficult to define, and different methods might differ from each other depending non-linearly on the environmental conditions (*49*).

3. Deduced HOM formation pathways in the presence of NO_x

NO_x can affect the HOM formation in many ways. We need to firstly consider how NO_x influenced the main oxidants of monoterpenes. The concentration of O_3 can be influenced in three channels: First, NO can reduce O_3 concentration by directly reacting with it; Second, NO_2 can produce O_3 via its photolysis, especially with the presence of RO_2 or HO_2 radicals that recycle NO back to NO_2; Third, NO_2 can also react with O_3 to form NO_3 radical, another important oxidant of monoterpenes (*50, 51*). Regarding to the O_3 concentration, Channel 1 was the most important, as we observed a net reduction of O_3, which was almost equivalent to the net production of NO_2. Although only a tiny amount of NO_3 was formed via Channel 3 in comparison to NO and NO_2, it had a considerable contribution to the production of HOMs, as

we will discuss below. The OH concentration can also be influenced in multiple ways: First, both NO and NO_2 directly react with OH, leading to a reduction of OH concentration; Second, NO can react with HO_2 the produce OH; Third, the OH production via monoterpene ozonolysis is influenced via affecting the O_3 concentration. The overall influence on OH concentration can be inferred from the change of H_2SO_4 concentration at the constant SO_2 concentration. In the conditions we focused on in this study, i.e., zero and 1.9 ppbv NO_x, the concentrations of O_3 and OH were not significantly affected: when 1.9 ppbv NO_x were injected, the O_3 and OH concentrations decreased by about 3 % and 10 %, respectively (Table S1).

After excluding a substantial decrease in OH and O_3 concentrations, the reduction of $C_xH_yO_{z\_di}$ can be mainly attributed to the reaction between NO_x and RO_2 (from the monoterpene oxidized by O_3 and OH) (*19*), competing with the suggested dimer formation via the accretion reaction of two RO_2 (*52, 53*). Meanwhile, this reaction also leads to the formation of $C_xH_yO_zN_{\_mono}$. Under most of our chamber conditions, NO, NO_2 and NO_3 were positively correlated, so their relative contribution cannot be easily distinguished with a single experiment. Because of this, we compare the HOM composition in two runs (Run1752 and Run1768, see Table S1) – the latter had a similar level of NO_2 but no NO. The concentration of $C_xH_yO_zN_{\_mono}$ formed in the Run1768 was much lower (~ 30 %) than that in the Run1752 (see Table S1), suggesting that the reaction of NO + RO_2 is a more efficient pathway of forming organic nitrate monomers. This means the traditional knowledge of RO_2 chemistry still applies to these highly oxygenated RO_2, that NO + RO_2 forms stable organic nitrates but NO_2 only reacts with acylperoxy radicals forming peroxy nitrates (PANs) that are thermally unstable (*54*).

In addition, the NO_3-initiated oxidation had a considerable contribution, indicated by the formation of $C_xH_yO_zN_{2\_mono}$, $C_xH_yO_zN_{\_di}$, and $C_xH_yO_zN_{2\_di.}$ Meanwhile, this pathway may also lead to the formation of $C_xH_yO_zN_{1\_mono}$, which however, cannot be distinguished from the products via NO_x+RO_2 pathways. Similar to our recent findings at the reference station (*55*), we attribute the formation of $C_xH_yO_zN_{\_di}$ and $C_xH_yO_zN_{2\_di}$ to the RO_2 + RO_2· reactions, with one or both parent RO_2 being produced by the NO_3-initiated oxidation. In addition, we also attribute the formation of $C_xH_yO_zN_{2\_mono}$, exclusively observed as $C_{10}H_{16}O_xN_2$, to a combination of NO_3-initiated oxidation followed by a termination reaction with NO. This formation pathway explains two features of these molecules: 1) the two nitrogen atoms are introduced by NO_3 oxidation and NO termination, respectively, and 2) there is no hydrogen gain or loss, as the number of hydrogen atoms in these products is the same as in the monoterpene precursors. It seems that NO_2 is not involved in the formation of $C_xH_yO_zN_{2\_mono}$ (Fig. S*7*), most likely because the acylperoxy radicals are rarely formed from the NO_3-initiated oxidation (*56*). As previously shown, the HOM yields from the NO_3-initiated

oxidation of different monoterpenes may vary significantly (*51*), and the formation of highly oxygenated RO_2 is favored in NO_3 oxidizing Δ-3-carene but disfavored in the α-pinene case (*56*). Therefore, the NO_3-related HOMs in this study might mainly come from the oxidation of Δ-3-carene. Overall, in this chosen experiment, at 1.9 ppbv NO_x, NO_3-initiated oxidation contributes to at least about 10% (Fig. 2b, the sum of fractions of $C_xH_yO_zN_{1\text{-}2\_di}$ and $C_xH_yO_zN_{2\_mono}$, but disregarding the plausible fraction of $C_xH_yO_zN_{\_mono}$) of the total HOMs and about 30% of the HOM dimers (sum of $C_xH_yO_zN_{1\text{-}2\_di}$ fractions over the total dimer fraction in Fig. 2b).

4. Volatility estimation

As shown in the manuscript, the previously reported volatility parameterization (*14*) can be extended to include all types of HOMs by using the $O{:}C_{eff}$. This parameterization is based on the volatility estimation of individual HOM molecule with the SIMPOL model (*57*). There also exists a few other approaches to estimate the HOM volatility, including the EVAPORATION group contribution method (*58, 59*), COSMOTherm (*60*), and a method to derive volatility from the thermogram measured with the FIGAERO inlet (*61*). Significant differences have been revealed in the absolute volatilities estimated between the different models. For example, it has been suggested that the EVAPORATION and SIMPOL models may underestimate the volatility due to the negligence of intramolecular H-bonds, whereas the COSMOTherm model seems to overestimate volatility (*60*). The thermogram method, on the other hand, gives even lower volatilities relative to the SIMPOL model, likely due to the thermal decomposition of the particle-phase oligomers (*29*). In the analysis of the thermograms in this work, we also found that thermal decomposition of HOM dimers interfered with the T_{max} of monomers.

Another important uncertainty of HOM volatility distribution comes from the use of different parameterizations. For example, different parameterizations, both based on SIMPOL model, were used in this work and by Stolzenburg and co-workers (*41*), meanwhile, another parameterization was derived by Li and co-workers based on the EVAPORATION model (*61*). We show in Fig. S8 the comparison of HOM volatility distributions estimated by these three parameterizations under both zero and 1.9 ppbv NO_x conditions. Despite of very different parameterizations, the HOM volatility distributions derived in this work and by Stolzenburg and co-workers are largely similar. On the other hand, the parameterization based on EVAPORATION gives lower volatility by about 3-4 orders of magnitude than what are predicted by the other two parameterizations. However, the fact that NO_x can cause the HOM volatility distribution shift to higher volatility can be seen from all parameterizations (Fig. S8

bottom panel). Therefore, the main finding of this work that adding NO_x substantially shifts the volatility to higher values is not affected by the parameterization chosen.

Supplementary figures

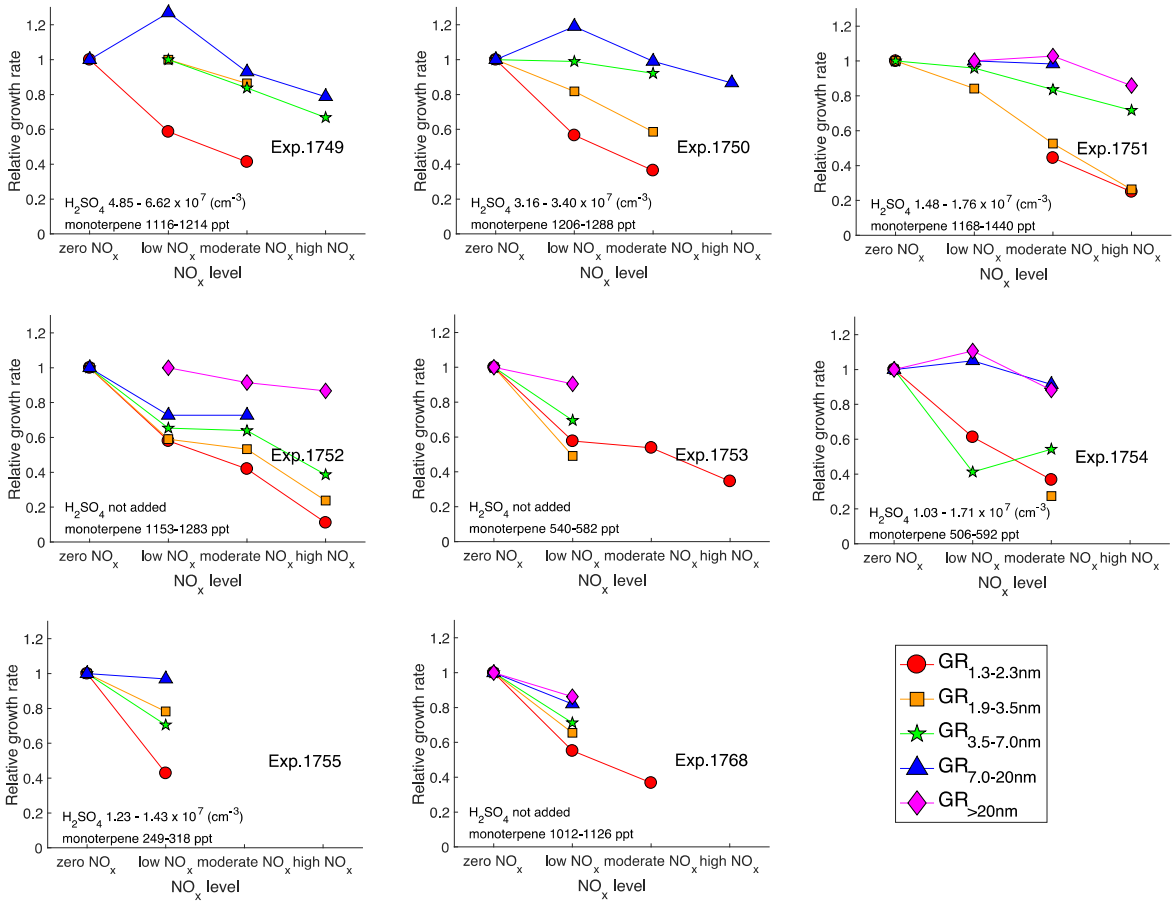

Fig. S1. Size-segregated particle growth rates suppressed by NO_x. Similar to the bottom panel of Fig.1, growth rates are normalized to those measured at the zero NO_x condition, so that the ratio shows the degree of suppression by NO_x. The original data are shown in Table S1.

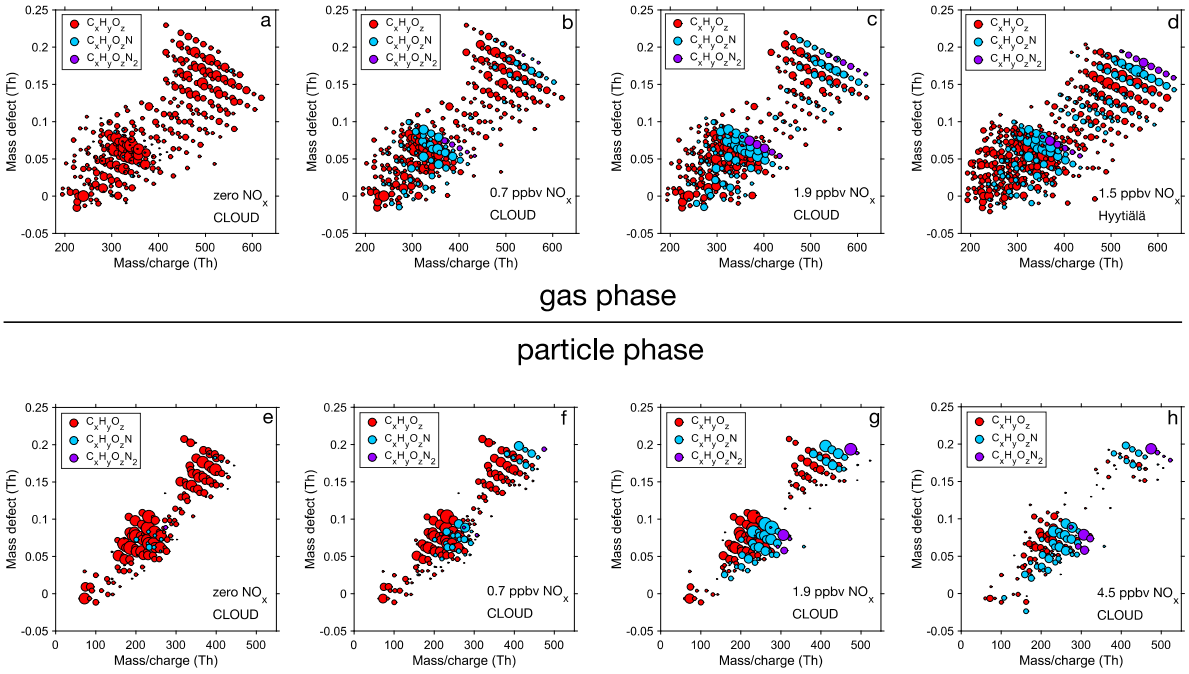

Fig. S2. HOMs measurements in gas phase and particle phase under different NO_x conditions. For all plots**,** the x-axis is the exact mass of HOMs, y-axis is the mass defect (the difference between the exact mass and the nominal mass), the color of plotted circles denotes the type of HOMs (i.e. how many nitrogen atoms the molecules contain), and the size of the plotted circles is proportional to the logarithm of the counting rate. Fig. S2 a,b,c,d are gas-phase HOMs measured with the nitrate CI-APi-TOF. Fig. S2 e,f,g,h show the HOMs measured in the particle phase with the FIGAERO inlet, in which signals of the deprotonated form ($C_xH_{y-1}O_z^-$) and cluster form ($C_xH_yO_zI^-$) are summed up.

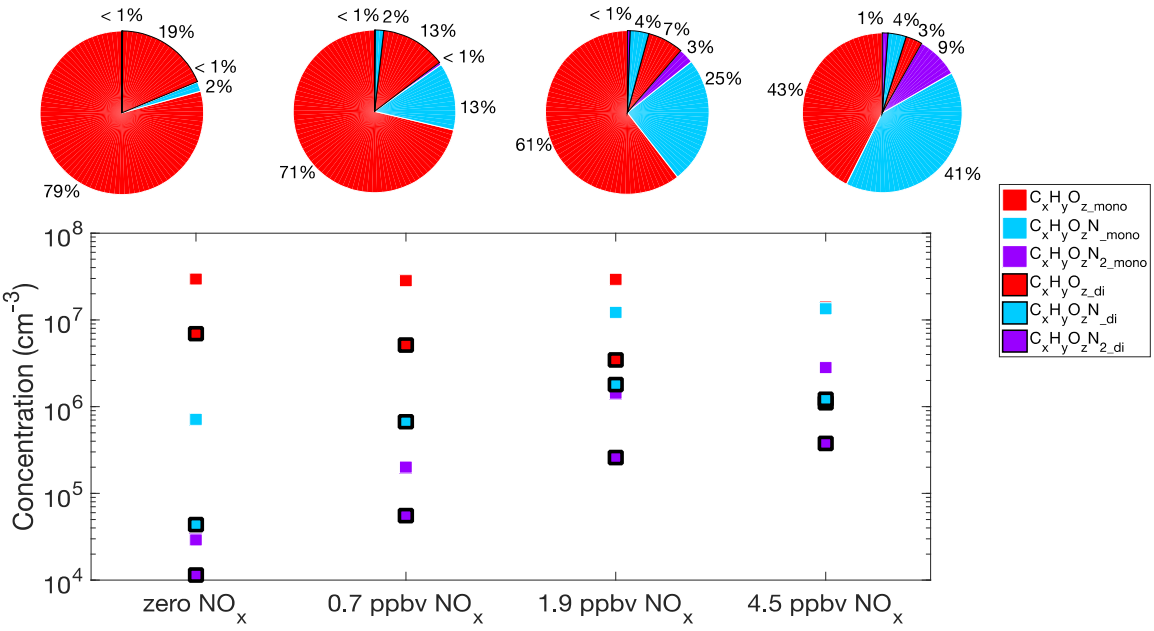

Fig. S3. The concentration and relative fraction of different types of HOMs at different NO_x levels. Mass spectrometer data are averaged based on the full course of each NO_x condition in order to maximize the accuracy of peak fitting. We provide both the exact concentration and the relative contribution of each type of HOMs. The first and third (from left) NO_x conditions are shown in Fig. 2 as examples.

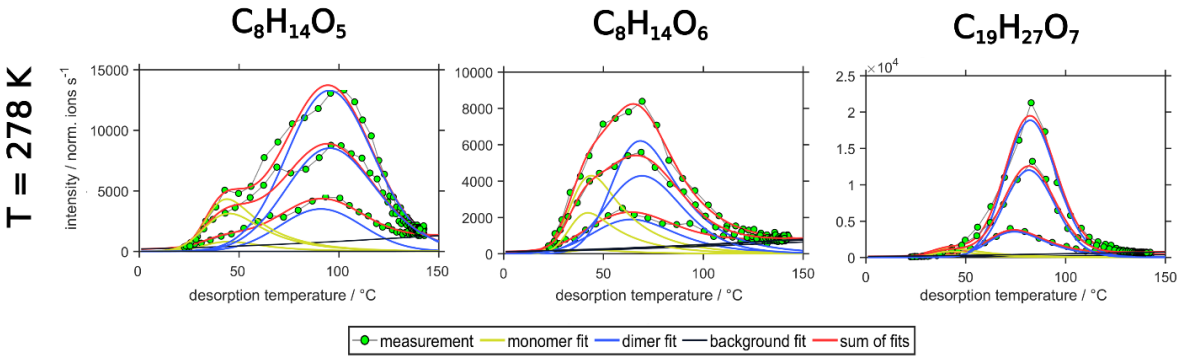

Fig. S4. Thermogram of example monomeric and dimer compounds. In our experiment, the thermogram of a monomeric compound is usually bimodal with a larger contribution from the thermal decomposition of dimeric compounds.

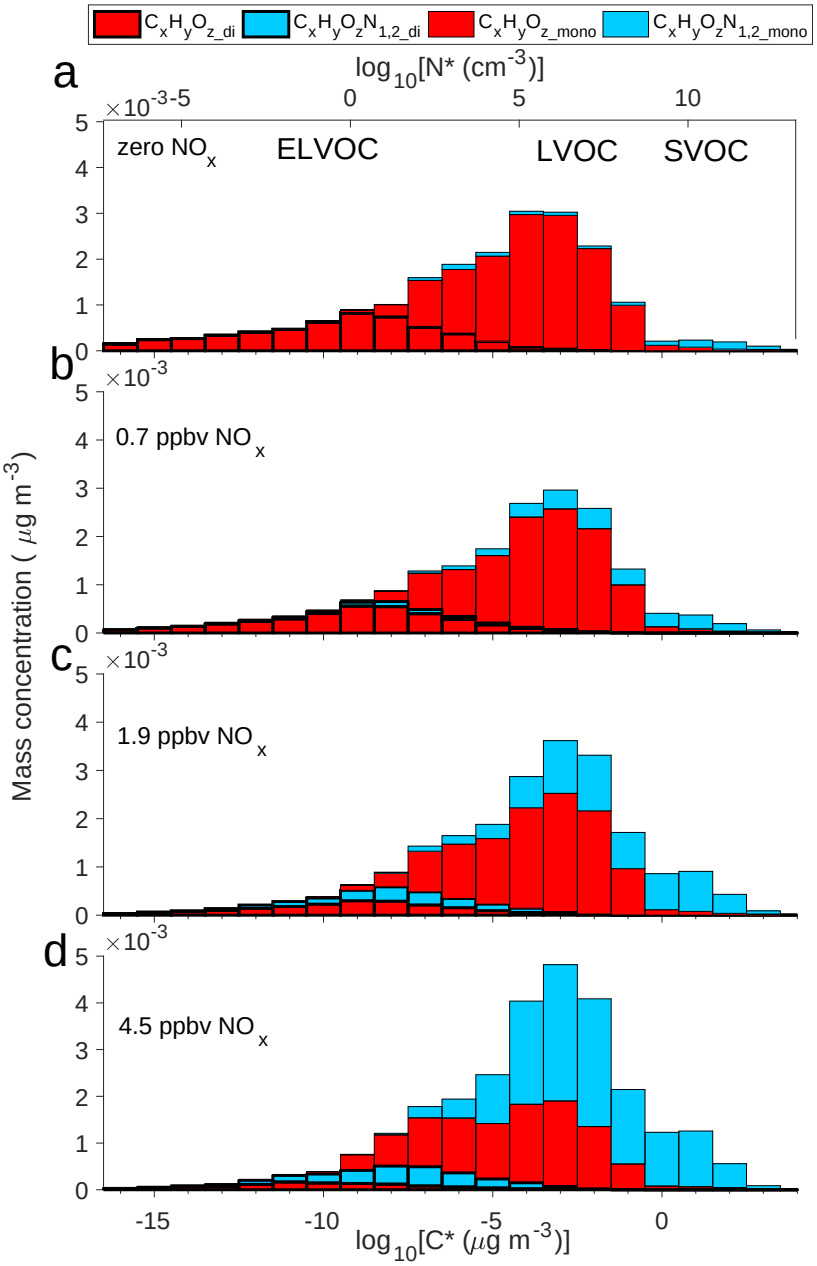

Fig. S5. Mass concentration and volatility distribution of HOMs under different NO_x conditions. Dimers are marked by the black frame; blue and red bars denote HOMs with and without nitrate group, respectively; HOMs contain one or two nitrate groups are not separated.

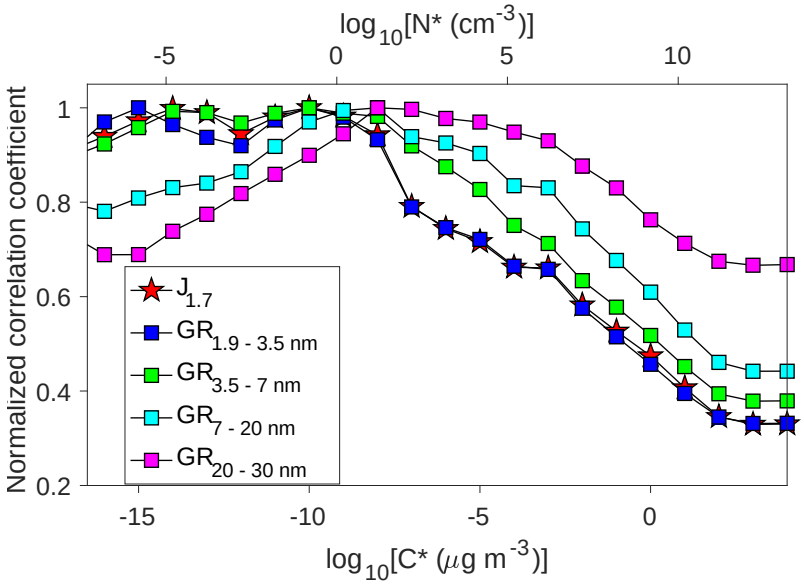

Fig. S6. Normalized correlation coefficient of particle nucleation rate ($J_{1.7}$) and size-segregated growth rates ($GR_{1.9\text{-}3.5\ nm}$, $GR_{3\text{-}7\ nm}$, $GR_{7\text{-}20\ nm}$, and $GR_{20\text{-}30\ nm}$) with cumulative HOM concentration. The growth rate contributed by H_2SO_4 condensation is calculated based on the equation derived by Nieminen and co-workers (*62*) and subtracted from the measured values.

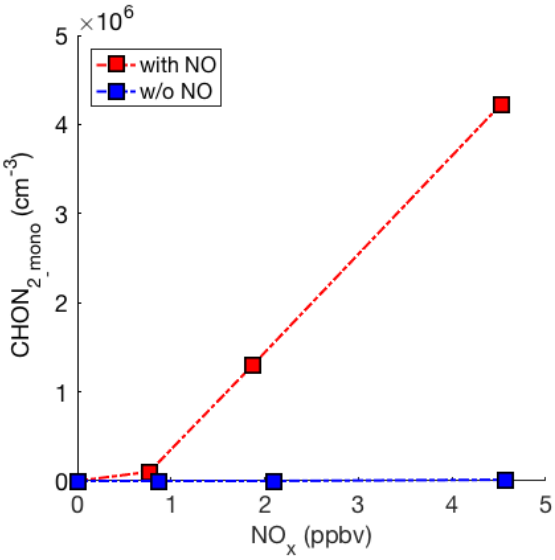

Fig. S7. The effect of NO in $C_xH_yO_zN_{2\_mono}$ formation. The blue and red are used to denote conditions without (Run1768) and with NO (Run1752). This confirms that NO is involved in the formation of this type of HOMs.

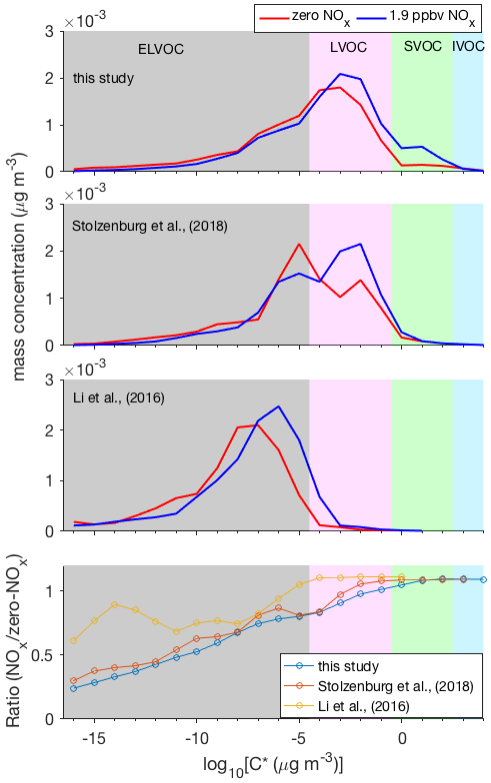

Fig. S8. HOM volatility distributions using three different parameterization and their respective changes led by NO_x. The top three panels show the distributions and the bottom panel gives the ratio of cumulative HOM concentrations.

Table S1. Summary of experimental conditions, the respective concentrations of gaseous species (a), and the determined size-dependent particle growth rates (b). *without injection; ** NO_2 only (without NO)

Table S1a

Exp.	Ozone (ppbv)	MT (pptv)	SO_2 (ppbv)	NO_x (ppbv)	H_2SO_4 (cm^{-3})	CHO_{mono} (cm^{-3})	$CHON_{1\text{-}2\ mono}$ (cm^{-3})	CHO_{di} (cm^{-3})	$CHON_{1\text{-}2\ di}$ (cm^{-3})
1748	39.8	594	3.2	-*	6.55E+07	1.75E+07	1.20E+06	2.59E+06	2.30E+05
	40.4	574	3.3	0.32	7.05E+07	1.77E+07	4.10E+06	1.96E+06	8.85E+05
	39.3	556	3.3	1.88	5.69E+07	1.76E+07	1.07E+07	1.29E+06	1.40E+06
	36.3	540	3.4	4.69	4.62E+07	1.77E+07	1.76E+07	8.22E+05	1.11E+06
1749	40.6	1166	3.4	-*	6.62E+07	2.64E+07	6.12E+05	4.57E+06	1.15E+05
	39.8	1281	3.3	0.57	5.99E+07	2.76E+07	4.50E+06	3.92E+06	1.00E+06
	38.7	1244	3.3	1.63	5.18E+07	2.47E+07	1.03E+07	2.36E+06	1.50E+06
	36.8	1214	3.3	4.35	4.85E+07	2.68E+07	2.24E+07	1.58E+06	1.82E+06
1750	40.3	1288	2.0	-*	3.40E+07	2.71E+07	5.22E+05	5.11E+06	1.90E+05
	39.9	1274	2.0	0.612	3.29E+07	2.56E+07	4.00E+06	3.67E+06	8.60E+05
	38.8	1241	2.0	1.68	3.35E+07	2.57E+07	1.11E+07	2.57E+06	1.65E+06
	36.2	1206	2.0	4.24	3.16E+07	2.66E+07	2.38E+07	1.66E+06	1.95E+06
1751	38.8	1440	1.0	-*	1.48E+07	2.18E+07	4.35E+05	4.51E+06	1.47E+05
	39.4	1276	1.0	0.79	1.66E+07	2.40E+07	3.37E+06	3.72E+06	7.43E+05
	38.5	1212	1.0	1.80	1.76E+07	2.52E+07	1.06E+07	2.60E+06	1.68E+06
	35.8	1168	1.0	4.57	1.63E+07	2.62E+07	2.41E+07	1.64E+06	2.06E+06
1752	39.9	1274	-*	-*	-	2.94E+07	6.34E+05	7.23E+06	9.53E+04
	39.7	1283	-*	0.77	-	2.60E+07	3.96E+06	4.21E+06	8.92E+05
	38.9	1211	-*	1.87	-	2.68E+07	1.25E+07	2.96E+06	1.81E+06
	35.7	1153	-*	4.52	-	2.54E+07	2.35E+07	1.73E+06	2.46E+06
1753	34.3	546	-*	4.82	-	1.71E+07	1.25E+07	1.20E+06	1.02E+06
	38.1	540	-*	1.84	-	1.45E+07	9.65E+06	1.23E+06	1.46E+06
	39.7	569	-*	0.68	-	1.63E+07	3.98E+06	2.03E+06	1.04E+06
	40.9	582	-*	-*	-	1.70E+07	1.20E+06	2.99E+06	4.26E+05
1754	40.2	592	1.0	-*	1.69E+07	1.29E+07	7.98E+05	2.49E+06	1.33E+05
	40.0	575	1.0	0.77	1.71E+07	1.40E+07	3.18E+06	1.76E+06	7.58E+05
	39.3	535	1.0	1.88	1.48E+07	1.33E+07	8.18E+06	1.05E+06	1.27E+06
	35.8	506	1.1	4.59	1.03E+07	1.02E+07	9.72E+06	5.53E+05	8.16E+05
1755	40.1	318	1.1	-*	1.43E+07	1.07E+07	8.23E+05	1.48E+06	1.29E+05
	40.0	286	1.1	0.69	1.37E+07	9.63E+06	3.17E+06	8.28E+05	6.67E+05
	38.8	251	1.1	1.99	1.28E+07	8.52E+06	6.94E+06	5.48E+05	7.71E+05
	36.9	249	1.1	3.90	1.23E+07	8.62E+06	9.22E+06	4.16E+05	5.42E+05
1768	41.8	1126	-*	-**	-	2.55E+07	1.27E+06	6.24E+06	1.99E+05
	41.6	1135	-*	0.83**	-	2.02E+07	2.29E+06	4.61E+06	1.09E+06
	41.6	1068	-*	2.10**	-	1.68E+07	3.75E+06	3.28E+06	2.39E+06
	40.9	1012	-*	4.57**	-	1.20E+07	4.64E+06	2.06E+06	2.92E+06

Table S1b

Exp.	$GR_{1.3\text{-}2.3\ nm}$ (nm/h)	$GR_{1.9\text{-}3.5\ nm}$ (nm/h)	$GR_{3.5\text{-}7\ nm}$ (nm/h)	$GR_{7\text{-}20\ nm}$ (nm/h)	$GR_{>20\ nm}$ (nm/h)
1748	6.7	4.1	17.8	15.1	-
	-	-	-	-	-
	-	-	-	-	-
	-	-	-	-	-
1749	13.3	-	-	21.2	-
	7.8	15.4	25.9	26.9	-
	5.5	13.3	21.7	19.7	-
	-	-	17.3	16.7	-
1750	12.9	9.9	19.1	21.0	-
	7.3	8.1	18.9	25.0	-
	4.7	5.8	17.6	20.8	-
	-	-	-	18.2	-
1751	7.2	11.4	21.9	-	-
	-	9.6	21	18.1	14.2
	3.2	6.0	18.3	17.8	14.6
	1.8	3.0	15.7	-	12.2
1752	8.1	12.2	20.2	22.0	-
	4.7	7.2	13.2	16.0	14.1
	3.4	6.5	12.9	16.0	12.9
	0.9	2.9	7.8	-	12.23
1753	2.6	5.7	9.2	-	8.4
	1.5	2.8	6.4	-	7.6
	1.4	-	-	-	-
	0.9	-	-	-	-
1754	4.9	14.6	15.3	14.0	8.5
	3.0	-	6.3	14.7	9.4
	1.8	4	8.3	12.8	7.5
	-	-	-	-	-
1755	1.4	2.3	7.8	6.4	-
	0.6	1.8	5.5	6.2	-
	-	-	-	-	-
	-	-	-	-	-
1768	8.7	11.3	20.5	24.5	21.1
	4.8	7.4	14.6	20.1	18.2
	3.2	-	-	-	-
	-	-	-	-	-

Table S2. Summary of main HOM formation pathways in the presence of NO_x.

Type of HOMs	Suggested main oxidant	Suggested main RO_2 terminator	Fingerprint molecules	References
$C_xH_yO_{z\_mono}$	O_3, OH	RO_2, HO_2, self-decomposition	$C_{10}H_{14,16}O_{7\text{-}11}$	e.g., (17, 34, 39, 63)
$C_xH_yO_zN_{\_mono}$	O_3, OH	NO (main), NO_2	$C_{10}H_{15}O_{7,9,11}N$	e.g., (55, *64*) this study
	NO_3	RO_2, HO_2, self-decomposition		
$C_xH_yO_zN_{2\_mono}$	NO_3	NO	$C_{10}H_{16}O_{9,11}N_2$	this study
$C_xH_yO_{z\_di}$	O_3, OH	RO_2	$C_{20}H_{32}O_{10,11,12}$	(14, *17*, *53*)
$C_xH_yO_zN_{\_di}$	NO_3	RO_2	$C_{20}H_{31}O_{11\text{-}13}N$	(55)
	O_3, OH	$R(NO_3)O_2$		
$C_xH_yO_zN_{2\_di}$	NO_3	$R(NO_3)O_2$	$C_{20}H_{32}O_{10,12}N_2$	(55)

REFERENCES AND NOTES

1. J. Merikanto, D. V. Spracklen, G. W. Mann, S. J. Pickering, K. S. Carslaw, Impact of nucleation on global CCN. *Atmos. Chem. Phys.* **9**, 8601–8616 (2009).

2. O. Boucher, D. Randall, P. Artaxo, C. Bretherton, G. Feingold, P. Forster, V.-M. Kerminen, Y. Kondo, H. Liao, U. Lohmann, P. Rasch, S. K. Satheesh, S. Sherwood, B. Stevens, X. Y. Zhang, *Climate Change 2013: The Physical Science Basis. Contribution of Working Group I to the Fifth Assessment Report of the Intergovernmental Panel on Climate Change*. (Cambridge Univ. Press, 2013), pp. 571–657.

3. M. Kulmala, J. Kontkanen, H. Junninen, K. Lehtipalo, H. E. Manninen, T. Nieminen, T. Petäjä, M. Sipilä, S. Schobesberger, P. Rantala, A. Franchin, T. Jokinen, E. Järvinen, M. Äijälä, J. Kangasluoma, J. Hakala, P. P. Aalto, P. Paasonen, J. Mikkilä, J. Vanhanen, J. Aalto, H. Hakola, U. Makkonen, T. Ruuskanen, R. L. Mauldin III, J. Duplissy, H. Vehkamäki, J. Bäck, A. Kortelainen, I. Riipinen, T. Kurtén, M. V. Johnston, J. N. Smith, M. Ehn, T. F. Mentel, K. E. J. Lehtinen, A. Laaksonen, V.-M. Kerminen, D. R. Worsnop, Direct observations of atmospheric aerosol nucleation. *Science* **339**, 943–946 (2013).

4. H. Vehkamäki, I. Riipinen, Thermodynamics and kinetics of atmospheric aerosol particle formation and growth. *Chem. Soc. Rev.* **41**, 5160–5173 (2012).

5. P. H. Mcmurry, M. Fink, H. Sakurai, M. R. Stolzenburg, R. L. Mauldin III, J. Smith, F. Eisele, K. Moore, S. Sjostedt, D. Tanner, L. G. Huey, J. B. Nowak, E. Edgerton, D. Voisin, A criterion for new particle formation in the sulfur–rich Atlanta atmosphere. *J. Geophys. Res. Atmos.* **110**, 2935–2948 (2005).

6. F. Riccobono, S. Schobesberger, C. E. Scott, J. Dommen, I. K. Ortega, L. Rondo, J. Almeida, A. Amorim, F. Bianchi, M. Breitenlechner, A. David, A. Downard, E. M. Dunne, J. Duplissy, S. Ehrhart, R. C. Flagan, A. Franchin, A. Hansel, H. Junninen, M. Kajos, H. Keskinen, A. Kupc, A. Kürten, A. N. Kvashin, A. Laaksonen, K. Lehtipalo, V. Makhmutov, S. Mathot, T. Nieminen, A. Onnela, T. Petäjä, A. P. Praplan, F. D. Santos, S. Schallhart, J. H. Seinfeld, M. Sipilä, D. V. Spracklen, Y. Stozhkov, F. Stratmann, A. Tomé, G. Tsagkogeorgas, P. Vaattovaara, Y. Viisanen, A. Vrtala, P. E. Wagner, E. Weingartner, H. Wex, D. Wimmer, K. S. Carslaw, J. Curtius, N. M. Donahue, J. Kirkby, M. Kulmala, D. R. Worsnop, U. Baltensperger, Oxidation products of biogenic emissions contribute to nucleation of atmospheric particles. *Science* **344**, 717–721 (2014).

7. R. Zhang, I. Suh, J. Zhao, D. Zhang, E. C. Fortner, X. Tie, L. T. Molina, M. J. Molina, Atmospheric new particle formation enhanced by organic acids. *Science* **304**, 1487–1490 (2004).

8. I. Riipinen, J. R. Pierce, T. Yli-Juuti, T. Nieminen, S. Häkkinen, M. Ehn, H. Junninen, K. Lehtipalo, T. Petäjä, J. Slowik, R. Chang, N. C. Shantz, J. Abbatt, W. R. Leaitch, V.-M. Kerminen, D.-R. Worsnop, S. N. Pandis, N. M. Donahue, M. Kulmala, Organic condensation: A vital link connecting aerosol formation to cloud condensation nuclei (CCN) concentrations. *Atmos. Chem. Phys.* **11**, 3865–3878 (2011).

9. J. N. Smith, M. J. Dunn, T. M. Van Reken, K. Iida, M. R. Stolzenburg, P. H. McMurry, L. G. Huey, Chemical composition of atmospheric nanoparticles formed from nucleation in Tecamac, Mexico: Evidence for an important role for organic species in nanoparticle growth. *Geophys. Res. Lett.* **35**, 228–236 (2008).

10. N. M. Donahue, J. H. Kroll, S. N. Pandis, A. L. Robinson, A two-dimensional volatility basis set—Part 2: Diagnostics of organic-aerosol evolution. *Atmos. Chem. Phys.* **12**, 615–634 (2012).

11. K. Lehtipalo, C. Yan, L. Dada, F. Bianchi, M. Xiao, R. Wagner, D. Stolzenburg, L. R. Ahonen, A. Amorim, A. Baccarini, P. S. Bauer, B. Baumgartner, A. Bergen, A.-K. Bernhammer, M. Breitenlechner, S. Brilke, A. Buchholz, S. B. Mazon, D. Chen, X. Chen, A. Dias, J. Dommen, D. C. Draper, J. Duplissy, M. Ehn, H. Finkenzeller, L. Fischer, C. Frege, C. Fuchs, O. Garmash, H. Gordon, J. Hakala, X. He, L. Heikkinen, M. Heinritzi, J. C. Helm, V. Hofbauer, C. R. Hoyle, T. Jokinen, J. Kangasluoma, V.-M. Kerminen, C. Kim, J. Kirkby, J. Kontkanen, A. Kürten, M. J. Lawler, H. Mai, S. Mathot, R. L. Mauldin III, U. Molteni, L. Nichman, W. Nie, T. Nieminen, A. Ojdanic, A. Onnela, M. Passananti, T. Petäjä, F. Piel, V. Pospisilova, L. L. J. Quéléver, M. P. Rissanen, C. Rose, N. Sarnela, S. Schallhart, S. Schuchmann, K. Sengupta, M. Simon, M. Sipilä, C. Tauber, A. Tomé, J. Tröstl, O. Väisänen, A. L. Vogel, R. Volkamer, A. C. Wagner, M. Wang, L. Weitz, D. Wimmer, P. Ye, A. Ylisirniö, Q. Zha, K. S. Carslaw, J. Curtius, N. M. Donahue, R. C. Flagan, A. Hansel, I. Riipinen, A. Virtanen, P. M. Winkler, U. Baltensperger, M. Kulmala, D. R. Worsnop, Multicomponent new particle formation from sulfuric acid, ammonia, and biogenic vapors. *Sci. Adv.* **4**, eaau5363 (2018).

12. J. Kirkby, J. Duplissy, K. Sengupta, C. Frege, H. Gordon, C. Williamson, M. Heinritzi, M. Simon, C. Yan, J. Almeida, J. Tröstl, T. Nieminen, I. K. Ortega, R. Wagner, A. Adamov, A. Amorim, A.-K. Bernhammer, F. Bianchi, M. Breitenlechner, S. Brilke, X. Chen, J. Craven, A. Dias, S. Ehrhart, R. C. Flagan, A. Franchin, C. Fuchs, R. Guida, J. Hakala, C. R. Hoyle, T. Jokinen, H. Junninen, J. Kangasluoma, J. Kim, M. Krapf, A. Kürten, A. Laaksonen, K. Lehtipalo, V. Makhmutov, S. Mathot, U. Molteni, A. Onnela, O. Peräkylä, F. Piel, T. Petäjä, A. P. Praplan, K. Pringle, A. Rap, N. A. D. Richards, I. Riipinen, M. P. Rissanen, L. Rondo, N. Sarnela, S. Schobesberger, C. E. Scott, J. H. Seinfeld, M. Sipilä, G. Steiner, Y. Stozhkov, F. Stratmann, A. Tomé, A. Virtanen, A. L. Vogel, A. C. Wagner, P. E. Wagner, E. Weingartner, D. Wimmer, P. M. Winkler, P. Ye, X. Zhang, A. Hansel, J. Dommen, N. M. Donahue, D. R. Worsnop, U. Baltensperger, M. Kulmala, K. S. Carslaw, J. Curtius, Ion-induced nucleation of pure biogenic particles. *Nature* **533**, 521–526 (2016).

13. N. M. Donahue, I. K. Ortega, W. Chuang, I. Riipinen, F. Riccobono, S. Schobesberger, J. Dommen, U. Baltensperger, M. Kulmala, D. R. Worsnop, H. Vehkamaki, How do organic vapors contribute to new-particle formation? *Faraday Discuss.* **165**, 91–104 (2013).

14. J. Tröstl, W. K. Chuang, H. Gordon, M. Heinritzi, C. Yan, U. Molteni, L. Ahlm, C. Frege, F. Bianchi, R. Wagner, M. Simon, K. Lehtipalo, C. Williamson, J. S. Craven, J. Duplissy, A. Adamov, J. Almeida, A.-K. Bernhammer, M. Breitenlechner, S. Brilke, A. Dias, S. Ehrhart, R. C. Flagan, A. Franchin, C. Fuchs, R. Guida, M. Gysel, A. Hansel, C. R. Hoyle, T. Jokinen, H. Junninen, J. Kangasluoma, H. Keskinen, J. Kim, M. Krapf, A. Kürten, A. Laaksonen, M. Lawler, M. Leiminger, S. Mathot, O. Möhler, T. Nieminen, A. Onnela, T. Petäjä, F. M. Piel, P. Miettinen, M. P. Rissanen,

L. Rondo, N. Sarnela, S. Schobesberger, K. Sengupta, M. Sipilä, J. N. Smith, G. Steiner, A. Tomè, A. Virtanen, A. C. Wagner, E. Weingartner, D. Wimmer, P. M. Winkler, P. Ye, K. S. Carslaw, J. Curtius, J. Dommen, J. Kirkby, M. Kulmala, I. Riipinen, D. R. Worsnop, N. M. Donahue, U. Baltensperger, The role of low-volatility organic compounds in initial particle growth in the atmosphere. *Nature* **533**, 527–531 (2016).

15. I. Riipinen, T. Yli-Juuti, J. R. Pierce, T. Petäjä, D. R. Worsnop, M. Kulmala, N. M. Donahue, The contribution of organics to atmospheric nanoparticle growth. *Nat. Geosci.* **5**, 453–458 (2012).

16. J. D. Crounse, L. B. Nielsen, S. Jørgensen, H. G. Kjaergaard, P. O. Wennberg, Autoxidation of organic compounds in the atmosphere. *J. Phys. Chem. Lett.* **4**, 3513–3520 (2013).

17. M. Ehn, J. A. Thornton, E. Kleist, M. Sipilä, H. Junninen, I. Pullinen, M. Springer, F. Rubach, R. Tillmann, B. Lee, F. Lopez-Hilfiker, S. Andres, I.-H. Acir, M. Rissanen, T. Jokinen, S. Schobesberger, J. Kangasluoma, J. Kontkanen, T. Nieminen, T. Kurtén, L. B. Nielsen, S. Jørgensen, H. G. Kjaergaard, M. Canagaratna, M. D. Maso, T. Berndt, T. Petäjä, A. Wahner, V.-M. Kerminen, M. Kulmala, D. R. Worsnop, J. Wildt, T. F. Mentel, A large source of low-volatility secondary organic aerosol. *Nature* **506**, 476–479 (2014).

18. M. Ehn, E. Kleist, H. Junninen, T. Petäjä, G. Lönn, S. Schobesberger, M. Dal Maso, A. Trimborn, M. Kulmala, D. R. Worsnop, A. Wahner, J. Wildt, T. F. Mentel, Gas phase formation of extremely oxidized pinene reaction products in chamber and ambient air. *Atmos. Chem. Phys.* **12**, 5113–5127 (2012).

19. J. J. Orlando, G. S. Tyndall, Laboratory studies of organic peroxy radical chemistry: An overview with emphasis on recent issues of atmospheric significance. *Chem. Soc. Rev.* **41**, 6294–6317 (2012).

20. J. H. Seinfeld, S. N. Pandis, *Atmospheric Chemistry and Physics: From Air Pollution to Climate Change* (John Wiley & Sons, 2012).

21. B. J. Finlayson-Pitts, J. N. Pitts Jr, *Atmospheric Chemistry: Fundamentals and Experimental Techniques* (Wiley, 1986).

22. J. Wildt, T. F. Mentel, A. Kiendler-Scharr, T. Hoffmann, S. Andres, M. Ehn, E. Kleist, P. Müsgen, F. Rohrer, Y. Rudich, M. Springer, R. Tillmann, A. Wahner, Suppression of new particle formation from monoterpene oxidation by NO_x. *Atmos. Chem. Phys.* **14**, 2789–2804 (2014).

23. D. Zhao, S. H. Schmitt, M. Wang, I.-H. Acir, R. Tillmann, Z. Tan, A. Novelli, H. Fuchs, I. Pullinen, R. Wegener, F. Rohrer, J. Wildt, A. Kiendler-Scharr, A. Wahner, T. F. Mentel, Effects of NO_x and SO_2 on the secondary organic aerosol formation from photooxidation of α-pinene and limonene. *Atmos. Chem. Phys.* **18**, 1611–1628 (2018).

24. E. Praske, R. V. Otkjær, J. D. Crounse, J. C. Hethcox, B. M. Stoltz, H. G. Kjaergaard, P. O. Wennberg, Atmospheric autoxidation is increasingly important in urban and suburban North America. *Proc. Natl. Acad. Sci. U.S.A.* **115**, 64–69 (2018).

25. H. O. Pye, E. L. D'Ambro, B. H. Lee, S. Schobesberger, M. Takeuchi, Y. Zhao, F. Lopez-Hilfiker, J. Liu, J. E. Shilling, J. Xing, R. Mathur, A. M. Middlebrook, J. Liao, A. Welti, M. Graus, C. Warneke,

J. A. de Gouw, J. S. Holloway, T. B. Ryerson, I. B. Pollack, J. A. Thornton, Anthropogenic enhancements to production of highly oxygenated molecules from autoxidation. *Proc. Natl. Acad. Sci. U.S.A.* **116**, 6641–6646 (2019).

26. J. Rinne, H. Hakola, T. Laurila, Ü. Rannik, Canopy scale monoterpene emissions of *Pinus sylvestris* dominated forests. *Atmos. Environ.* **34**, 1099–1107 (2000).

27. F. Bianchi, T. Kurtén, M. Riva, C. Mohr, M. P. Rissanen, P. Roldin, T. Berndt, J. D. Crounse, P. O. Wennberg, T. F. Mentel, J. Wildt, H. Junninen, T. Jokinen, M. Kulmala, D. R. Worsnop, J. A. Thornton, N. Donahue, H. G. Kjaergaard, M. Ehn, Highly oxygenated organic molecules (HOM) from gas-phase autoxidation involving peroxy radicals: A key contributor to atmospheric aerosol. *Chem. Rev.* **119**, 3472–3509 (2019).

28. W. K. Chuang, N. M. Donahue, A two-dimensional volatility basis set—Part 3: Prognostic modeling and NO_x dependence. *Atmos. Chem. Phys.* **16**, 123–134 (2016).

29. H. Stark, R. L. N. Yatavelli, S. L. Thompson, H. Kang, J. E. Krechmer, J. R. Kimmel, B. B. Palm, W. Hu, P. L. Hayes, D. A. Day, P. Campuzano-Jost, M. R. Canagaratna, J. T. Jayne, D. R. Worsnop, J. L. Jimenez, Impact of thermal decomposition on thermal desorption instruments: Advantage of thermogram analysis for quantifying volatility distributions of organic species. *Environ. Sci. Technol.* **51**, 8491–8500 (2017).

30. H. Wang, K. Lu, X. Chen, Q. Zhu, Q. Chen, S. Guo, M. Jiang, X. Li, D. Shang, Z. Tan, Y. Wu, Z. Wu, Q. Zou, Y. Zheng, L. Zeng, T. Zhu, M. Hu, Y. Zhang, High N_2O_5 concentrations observed in urban Beijing: Implications of a large nitrate formation pathway. *Environ. Sci. Technol. Lett.* **4**, 416–420 (2017).

31. A. Kiendler-Scharr, A. A. Mensah, E. Friese, D. Topping, E. Nemitz, A. S. H. Prevot, M. Äijälä, J. Allan, F. Canonaco, M. Canagaratna, S. Carbone, M. Crippa, M. Dall Osto, D. A. Day, P. De Carlo, C. F. Di Marco, H. Elbern, A. Eriksson, E. Freney, L. Hao, H. Herrmann, L. Hildebrandt, R. Hillamo, J. L. Jimenez, A. Laaksonen, G. McFiggans, C. Mohr, C. O'Dowd, R. Otjes, J. Ovadnevaite, S. N. Pandis, L. Poulain, P. Schlag, K. Sellegri, E. Swietlicki, P. Tiitta, A. Vermeulen, A. Wahner, D. Worsnop, H.-C. Wu, Ubiquity of organic nitrates from nighttime chemistry in the European submicron aerosol. *Geophys. Res. Lett.* **43**, 7735–7744 (2016).

32. M. H. Barley, D. Topping, D. Lowe, S. Utembe, G. McFiggans, The sensitivity of secondary organic aerosol (SOA) component partitioning to the predictions of component properties—Part 3: Investigation of condensed compounds generated by a near-explicit model of VOC oxidation. *Atmos. Chem. Phys.* **11**, 13145–13159 (2011).

33. T. Moise, J. M. Flores, Y. Rudich, Optical properties of secondary organic aerosols and their changes by chemical processes. *Chem. Rev.* **115**, 4400–4439 (2015).

34. T. Jokinen, T. Berndt, R. Makkonen, V.-M. Kerminen, H. Junninen, P. Paasonen, F. Stratmann, H. Herrmann, A. B. Guenther, D. R. Worsnop, M. Kulmala, M. Ehn, M. Sipilä, Production of extremely low volatile organic compounds from biogenic emissions: Measured yields and atmospheric implications. *Proc. Natl. Acad. Sci. U.S.A.* **112**, 7123–7128 (2015).

35. T. Jokinen, M. Sipilä, H. Junninen, M. Ehn, G. Lönn, J. Hakala, T. Petäjä, R. L. Mauldin III, M. Kulmala, D. R. Worsnop, Atmospheric sulphuric acid and neutral cluster measurements using CI-APi-TOF. *Atmos. Chem. Phys.* **12**, 4117–4125 (2012).

36. H. Junninen, M. Ehn, T. Petäjä, L. Luosujärvi, T. Kotiaho, R. Kostiainen, U. Rohner, M. Gonin, K. Fuhrer, M. Kulmala, D. R. Worsnop, A high-resolution mass spectrometer to measure atmospheric ion composition. *Atmos. Meas. Tech.* **3**, 1039–1053 (2010).

37. M. Heinritzi, M. Simon, G. Steiner, A. C. Wagner, A. Kürten, A. Hansel, J. Curtius, Characterization of the mass-dependent transmission efficiency of a CIMS. *Atmos. Meas. Tech.* **9**, 1449–1460 (2016).

38. N. Hyttinen, O. Kupiainen-Määttä, M. P. Rissanen, M. Muuronen, M. Ehn, T. Kurtén, Modeling the charging of highly oxidized cyclohexene ozonolysis products using nitrate-based chemical ionization. *J. Phys. Chem. A* **119**, 6339–6345 (2015).

39. T. Berndt, S. Richters, T. Jokinen, N. Hyttinen, T. Kurtén, R. V. Otkjær, H. G. Kjaergaard, F. Stratmann, H. Herrmann, M. Sipilä, M. Kulmala, M. Ehn, Hydroxyl radical-induced formation of highly oxidized organic compounds. *Nat. Commun.* **7**, 13677 (2016).

40. F. D. Lopez-Hilfiker, C. Mohr, M. Ehn, F. Rubach, E. Kleist, J. Wildt, T. F. Mentel, A. Lutz, M. Hallquist, D. Worsnop, J. A. Thornton, A novel method for online analysis of gas and particle composition: Description and evaluation of a Filter Inlet for Gases and AEROsols (FIGAERO). *Atmos. Meas. Tech.* **7**, 983–1001 (2014).

41. D. Stolzenburg, L. Fischer, A. L. Vogel, M. Heinritzi, M. Schervish, M. Simon, A. C. Wagner, L. Dada, L. R. Ahonen, A. Amorim, A. Baccarini, P. S. Bauer, B. Baumgartner, A. Bergen, F. Bianchi, M. Breitenlechner, S. Brilke, S. Buenrostro Mazon, D. Chen, A. Dias, D. C. Draper, J. Duplissy, I. El Haddad, H. Finkenzeller, C. Frege, C. Fuchs, O. Garmash, H. Gordon, X. He, J. Helm, V. Hofbauer, C. R. Hoyle, C. Kim, J. Kirkby, J. Kontkanen, A. Kürten, J. Lampilahti, M. Lawler, K. Lehtipalo, M. Leiminger, H. Mai, S. Mathot, B. Mentler, U. Molteni, W. Nie, T. Nieminen, J. B. Nowak, A. Ojdanic, A. Onnela, M. Passananti, T. Petäjä, L. L. J. Quéléver, M. P. Rissanen, N. Sarnela, S. Schallhart, C. Tauber, A. Tomé, R. Wagner, M. Wang, L. Weitz, D. Wimmer, M. Xiao, C. Yan, P. Ye, Q. Zha, U. Baltensperger, J. Curtius, J. Dommen, R. C. Flagan, M. Kulmala, J. N. Smith, D. R. Worsnop, A. Hansel, N. M. Donahue, P. M. Winkler, Rapid growth of organic aerosol nanoparticles over a wide tropospheric temperature range. *Proc. Natl. Acad. Sci.* **115**, 9122–9127 (2018).

42. M. Breitenlechner, L. Fischer, M. Hainer, M. Heinritzi, J. Curtius, A. Hansel, PTR3: An instrument for studying the lifecycle of reactive organic carbon in the atmosphere. *Anal. Chem.* **89**, 5824–5831 (2017).

43. J. Vanhanen, J. Mikkilä, K. Lehtipalo, M. Sipilä, H. E. Manninen, E. Siivola, T. Petäjä, M. Kulmala, Particle size magnifier for nano-CN detection. *Aero. Sci. Technol.* **45**, 533–542 (2011).

44. K. Lehtipalo, J. Leppa, J. Kontkanen, J. Kangasluoma, A. Franchin, D. Wimnner, S. Schobesberger, H. Junninen, T. Petaja, M. Sipila, J. Mikkila, J. Vanhanen, D. R. Worsnop, M. Kulmala, Methods for

determining particle size distribution and growth rates between 1 and 3 nm using the Particle Size Magnifier. *Boreal Environ. Res.* **19**, 215–236 (2014).

45. D. Stolzenburg, G. Steiner, P. M. Winkler, A DMA-train for precision measurement of sub-10 nm aerosol dynamics. *Atmos. Meas. Tech.* **10**, 1639–1651 (2017).

46. S. Mirme, A. Mirme, The mathematical principles and design of the NAIS—A spectrometer for the measurement of cluster ion and nanometer aerosol size distributions. *Atmos. Meas. Tech.* **6**, 1061–1071 (2013).

47. J. Kangasluoma, A. Samodurov, M. Attoui, A. Franchin, H. Junninen, F. Korhonen, T. Kurtén, H. Vehkamäki, M. Sipilä, K. Lehtipalo, D. R. Worsnop, T. Petäjä, M. Kulmala, Heterogeneous nucleation onto ions and neutralized ions: Insights into sign-preference. *J. Phys. Chem. C* **120**, 7444–7450 (2016).

48. K. Lehtipalo, L. Rondo, J. Kontkanen, S. Schobesberger, T. Jokinen, N. Sarnela, A. Kürten, S. Ehrhart, A. Franchin, T. Nieminen, F. Riccobono, M. Sipilä, T. Yli-Juuti, J. Duplissy, A. Adamov, L. Ahlm, J. Almeida, A. Amorim, F. Bianchi, M. Breitenlechner, J. Dommen, A. J. Downard, E. M. Dunne, R. C. Flagan, R. Guida, J. Hakala, A. Hansel, W. Jud, J. Kangasluoma, V.-M. Kerminen, H. Keskinen, J. Kim, J. Kirkby, A. Kupc, O. Kupiainen-Määttä, A. Laaksonen, M. J. Lawler, M. Leiminger, S. Mathot, T. Olenius, I. K. Ortega, A. Onnela, T. Petäjä, A. Praplan, M. P. Rissanen, T. Ruuskanen, F. D. Santos, S. Schallhart, R. Schnitzhofer, M. Simon, J. N. Smith, J. Tröstl, G. Tsagkogeorgas, A. Tomé, P. Vaattovaara, H. Vehkamäki, A. E. Vrtala, P. E. Wagner, C. Williamson, D. Wimmer, P. M. Winkler, A. Virtanen, N. M. Donahue, K. S. Carslaw, U. Baltensperger, I. Riipinen, J. Curtius, D. R. Worsnop, M. Kulmala, The effect of acid–base clustering and ions on the growth of atmospheric nano-particles. *Nat. Commun.* **7**, 11594 (2016).

49. J. Kontkanen, T. Olenius, K. Lehtipalo, H. Vehkamäki, M. Kulmala, K. E. J. Lehtinen, Growth of atmospheric clusters involving cluster–cluster collisions: Comparison of different growth rate methods. *Atmos. Chem. Phys.* **16**, 5545–5560 (2016).

50. J. L. Fry, D. C. Draper, K. C. Barsanti, J. N. Smith, J. Ortega, P. M. Winkler, M. J. Lawler, S. S. Brown, P. M. Edwards, R. C. Cohen, L. Lee, Secondary organic aerosol formation and organic nitrate yield from NO_3 oxidation of biogenic hydrocarbons. *Environ. Sci. Technol.* **48**, 11944–11953 (2014).

51. N. L. Ng, S. S. Brown, A. T. Archibald, E. Atlas, R. C. Cohen, J. N. Crowley, D. A. Day, N. M. Donahue, J. L. Fry, H. Fuchs, R. J. Griffin, M. I. Guzman, H. Herrmann, A. Hodzic, Y. Iinuma, J. L. Jimenez, A. Kiendler-Scharr, B. H. Lee, D. J. Luecken, J. Mao, R. McLaren, A. Mutzel, H. D. Osthoff, B. Ouyang, B. Picquet-Varrault, U. Platt, H. O. T. Pye, Y. Rudich, R. H. Schwantes, M. Shiraiwa, J. Stutz, J. A. Thornton, A. Tilgner, B. J. Williams, R. A. Zaveri, Nitrate radicals and biogenic volatile organic compounds: Oxidation, mechanisms, and organic aerosol. *Atmos. Chem. Phys.* **17**, 2103–2162 (2017).

52. T. Berndt, W. Scholz, B. Mentler, L. Fischer, H. Herrmann, M. Kulmala, A. Hansel, Accretion product formation from self- and cross-reactions of RO_2 radicals in the atmosphere. *Angew. Chem. Int. Ed. Engl.* **57**, 3820–3824 (2018).

53. Y. Zhao, J. A. Thornton, H. O. T. Pye, Quantitative constraints on autoxidation and dimer formation from direct probing of monoterpene-derived peroxy radical chemistry. *Proc. Natl. Acad. Sci. U.S.A.* **115**, 12142–12147 (2018).

54. R. Atkinson, Rate constants for the atmospheric reactions of alkoxy radicals: An updated estimation method. *Atmos. Environ.* **41**, 8468–8485 (2007).

55. C. Yan, W. Nie, M. Äijälä, M. P. Rissanen, M. R. Canagaratna, P. Massoli, H. Junninen, T. Jokinen, N. Sarnela, S. A. K. Häme, S. Schobesberger, F. Canonaco, L. Yao, A. S. H. Prévôt, T. Petäjä, M. Kulmala, M. Sipilä, D. R. Worsnop, M. Ehn, Source characterization of highly oxidized multifunctional compounds in a boreal forest environment using positive matrix factorization. *Atmos. Chem. Phys.* **16**, 12715–12731 (2016).

56. T. Kurten, K. H. Møller, T. B. Nguyen, R. H. Schwantes, P. K. Misztal, L. Su, P. O. Wennberg, J. L. Fry, H. G. Kjaergaard, Alkoxy radical bond scissions explain the anomalously low secondary organic aerosol and organonitrate yields from α-Pinene + NO_3. *J. Phys. Chem. Lett.* **8**, 2826–2834 (2017).

57. J. F. Pankow, W. E. Asher, SIMPOL.1: A simple group contribution method for predicting vapor pressures and enthalpies of vaporization of multifunctional organic compounds. *Atmos. Chem. Phys.* **8**, 2773–2796 (2008).

58. S. Compernolle, K. Ceulemans, J.-F. Müller, EVAPORATION: A new vapour pressure estimation method for organic molecules including non-additivity and intramolecular interactions. *Atmos. Chem. Phys.* **11**, 9431–9450 (2011).

59. Y. Nannoolal, J. Rarey, D. Ramjugernath, Estimation of pure component properties: Part 3. Estimation of the vapor pressure of non-electrolyte organic compounds via group contributions and group interactions. *Fluid Phase Equilib.* **269**, 117–133 (2008).

60. T. Kurtén, K. Tiusanen, P. Roldin, M. Rissanen, J.-N. Luy, M. Boy, M. Ehn, N. Donahue, α-Pinene autoxidation products may not have extremely low saturation vapor pressures despite high O:C ratios. *J. Phys. Chem. A* **120**, 2569–2582 (2016).

61. Y. Li, U. Pöschl, M. Shiraiwa, Molecular corridors and parameterizations of volatility in the chemical evolution of organic aerosols. *Atmos. Chem. Phys.* **16**, 3327–3344 (2016).

62. T. Nieminen, K. E. J. Lehtinen, M. Kulmala, Sub-10 nm particle growth by vapor condensation—Effects of vapor molecule size and particle thermal speed. *Atmos. Chem. Phys.* **10**, 9773–9779 (2010).

63. T. F. Mentel, M. Springer, M. Ehn, E. Kleist, I. Pullinen, T. Kurtén, M. Rissanen, A. Wahner, J. Wildt, Formation of highly oxidized multifunctional compounds: Autoxidation of peroxy radicals formed in the ozonolysis of alkenes—Deduced from structure-product relationships. *Atmos. Chem. Phys.* **15**, 6745–6765 (2015).

64. B. H. Lee, C. Mohr, F. D. Lopez-Hilfiker, A. Lutz, M. Hallquist, L. Lee, P. Romer, R. C. Cohen, S. Iyer, T. Kurtén, W. Hu, D. A. Day, P. Campuzano-Jost, J. L. Jimenez, L. Xu, N. L. Ng, H. Guo, R. J.

Weber, R. J. Wild, S. S. Brown, A. Koss, J. de Gouw, K. Olson, A. H. Goldstein, R. Seco, S. Kim, K. McAvey, P. B. Shepson, T. Starn, K. Baumann, E. S. Edgerton, J. Liu, J. E. Shilling, D. O. Miller, W. Brune, S. Schobesberger, E. L. D'Ambro, J. A. Thornton, Highly functionalized organic nitrates in the southeast United States: Contribution to secondary organic aerosol and reactive nitrogen budgets. *Proc. Natl. Acad. Sci. U.S.A.* **113**, 1516–1521 (2016).